Continuous illumination picosecond imaging using a delay line detector in a transmission electron microscope

Teresa Weßels,[1,2] Simon Däster,[3] Yoshie Murooka,[1] Benjamin Zingsem,[4] Vadim Migunov,[1,5] Maximilan Kruth,[1] Simone Finizio,[6] Peng-Han Lu,[1] András Kovács,[1] Andreas Oelsner,[7] Knut Müller-Caspary,[1] Yves Acremann,[3] and Rafal E. Dunin-Borkowski[1]

[1]*Ernst Ruska-Centre for Microscopy and Spectroscopy with Electrons and Peter Grünberg Institute, Forschungszentrum Jülich, 52425 Jülich, Germany*

[2]*Lehrstuhl für Experimentalphysik IV E, RWTH Aachen University, 52056 Aachen, Germany*

[3]*Laboratory for Solid State Physics, ETH Zurich, 8093 Zurich, Switzerland*

[4]*Faculty of Physics and Center for Nanointegration (CENIDE), University of Duisburg-Essen, 47057 Duisburg, Germany*

[5]*Central Facility for Electron Microscopy (GFE), RWTH Aachen University, 52074 Aachen, Germany*

[6]*Swiss Light Source, Paul Scherrer Institut, 5232 Villigen PSI, Switzerland*

[7]*Surface Concept GmbH, 55124 Mainz, Germany*

Abstract

Progress towards analyzing transitions between steady states demands improvements in time-resolved imaging, both for fundamental research and for applications in information technology. Transmission electron microscopy is a powerful technique for investigating the atomic structure, chemical composition and electromagnetic properties of materials with high spatial resolution and precision. However, the extraction of information about dynamic processes in the ps time regime is often not possible without extensive modification to the instrument while requiring careful control of the operation conditions to not compromise the beam quality. Here, we avoid these drawbacks by combining a delay line detector with continuous illumination in a transmission electron microscope. We visualize the gyration of a magnetic vortex core in real space and show that magnetization dynamics up to frequencies of 2.3 GHz can be resolved with down to ∼122 ps temporal resolution by studying the interaction of an electron beam with a microwave magnetic field. In the future, this approach promises to provide access to resonant dynamics by combining high spatial resolution with sub-ns temporal resolution.

KEYWORDS

Imaging techniques, time-resolved transmission electron microscopy, ferromagnetism, Lorentz microscopy

1. INTRODUCTION

The ability to study magnetization dynamics on the nm scale is of great importance for both nanoelectronics and fundamental science. Developments such as racetrack memories [1], information transport by spin waves [2], the use of magnetic vortices as radio frequency sources [3] and the use of magnetic-vortex-based spin torque nano-oscillators as dynamic sensors [4] emphasize the importance of magnetization dynamics in future applications. Current methods of time-resolved magnetic imaging, such as those based on synchrotron X-rays [5, 6] and scanning electron microscopy with polarization analysis [7], allow the timescales of magneto-dynamic processes to be accessed through pump-probe imaging.

Magnetic imaging techniques based on transmission electron microscopy (TEM), such as Lorentz microscopy and off-axis electron holography, provide nm spatial resolution, even

with the sample located in magnetic-field-free conditions [8, 9], while offering complementary insight into the local microstructure and composition of the material [10]. However, the timescales of, *e.g.*, magnetic dynamics governed by the Landau-Lifshitz-Gilbert (LLG) equation, are on the order of 1 ps – 1 ns [11]. Whereas MHz and GHz resonances can be studied using X-rays with a typical spatial resolution of between 10 and 30 nm [12, 13], the temporal resolution of most conventional TEM techniques that are based on continuous illumination is currently in the ms range and hence six orders of magnitudes too low. Pump-probe TEM techniques based on the use of laser-driven photo-cathodes offer temporal resolutions down to the sub-picosecond [14–17]. However, they require extensive modification to the gun system of the microscope, such as the introduction of a laser system. In addition, careful control of the operation conditions is vital to not compromise the electron beam quality.

Here, we report a proof-of-principle study that demonstrates real-time ps observation of the gyration of a magnetic vortex core in a ferromagnetic thin film using a delay line detector (DLD) mounted on a spherical aberration corrected transmission electron microscope. A DLD is a high sensitivity, fast detector that has been used for imaging and spectroscopy over several decades in various scientific fields [18], but has only rarely been applied in electron microscopy. Recently, it has been employed for coincidence experiments correlating electron loss spectroscopy and energy dispersive X-ray spectroscopy [19]. The experiments that we describe below, which involve imaging a magnetic vortex core and electron diffraction, demonstrate a temporal resolution close to 100 ps and the ability to measure a beam deflection at a frequency of up to 2.3 GHz. We apply an in-plane magnetic field to a sample in the TEM by using a waveguide integrated in a single tilt TEM specimen holder, which can be operated over a frequency range of between DC and 40 GHz [20]. Our setup does not require any major modifications to the electron microscope, allowing electron beam coherence and spatial resolution to be maintained in both conventional and magnetic-field-free (Lorentz) imaging and diffraction. Moreover, the illumination is continuous and no pulsing is required to access magnetization dynamics.

2. EXPERIMENTAL DETAILS

The experimental setup is shown in Fig. 1. The sample is examined in an FEI Titan G2 60-300 TEM (300 kV), which is equipped with an objective lens aberration corrector and

a Gatan Tridiem 865 ER imaging filter [21]. The objective lens is turned off and a non-immersion Lorentz lens, which is situated below the sample, is used to provide the magnetic-field-free imaging conditions that are required to investigate magnetic vortex states. The conventional microscope objective lens is then used to apply out-of-plane, static magnetic fields to the sample. The sample studied here consists of a permalloy [(Py), $Ni_{81}Fe_{19}$ alloy] disk that has a thickness of 130 nm and a diameter of 1.68 μm and is patterned using electron beam lithography onto a 20 nm thick SiN membrane. Details about the patterning process are given in Ref. [22]. The disk was transferred in a focused ion beam workstation onto a chip that is compatible with a radio frequency (RF) specimen holder. As a result of the geometry and dimensions of the Py disk, it supports a magnetic vortex state with an out-of-plane core.

The magnetic vortex core was excited into motion about its equilibrium configuration with an in-plane RF magnetic field, as described in section 3 3.1 below. The RF generators (HP 8657B and HP 8671B) covered a frequency range of 100 MHz to 4 GHz. An amplifier (SPIN PA 233B A) was used to increase the RF current for all frequencies except for 100 MHz, with a total applied power of ∼20 dBm. In order to obtain temporal resolution, a frequency divider (developed in-house [23]) after the amplifier was used to divide the RF frequency by 64 to generate the starting signal of the DLD.

The DLD, which was provided by Surface Concept (single-anode delay line detector DLD4040) [18], was used to measure the positions and arrival times (x, y, t) of detected electrons, where t is the arrival time of each electron relative to an electronic starting signal. The DLD consists of a micro-channel plate (MCP), which generates a burst of secondary electrons for each detected primary electron. This burst is converted into a voltage pulse when it impacts an anode behind the MCP. In case of a delayline detector the anode consists of two stacked meandering waveguides, oriented perpendicular to each other. The electron burst from the MCP generates two voltage pulses on each meander, which propagate in opposite direction towards the detection electronics. By measuring the difference in arrival time at the ends of the meanders one can determine the position of the detected electron. The time measurement is performed by a time-to-digital converter (TDC). The average arrival time gives provides the arrival time of the electron. Therefore, a DLD provides three-dimensional information (x, y, t).

The TDC measures the arrival time of each electron in steps of $\tau = 6.858711$ ps after the

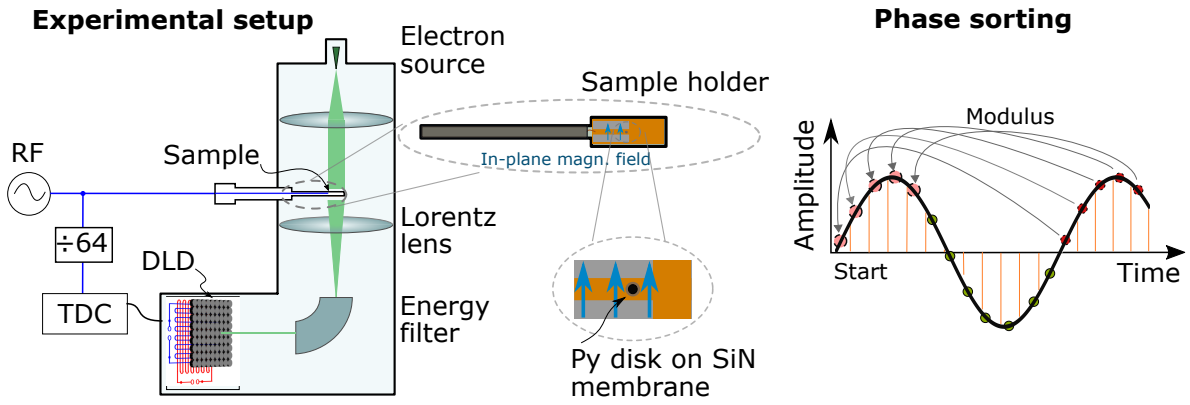

FIG. 1: Schematic diagram of the measurement setup and time binning used in the present study. (Left) The electron beam is deflected by a magnetic vortex core in a permalloy (Py) sample and imaged using a small area on the delay line detector (DLD). Two meanders on the detector record the times and positions of incoming electrons. Excitation of the magnetic vortex core and detection using the DLD are synchronized by using a frequency divider. (Right) The excitation cycle is divided into multiple steps. Steps corresponding to the same phase are summed up.

starting signal. The measured number of time steps $t_n = t/\tau$ was mapped onto one period of the RF signal by using a modulus operation, in the form of the number of time steps per RF period

$$m = \frac{1}{f_{RF}\tau} \quad , \tag{1}$$

where f_{RF} is the RF frequency. The resulting phase is $p_n = t_n \bmod m$ in units $\frac{2\pi}{p_n}$. The arrival time of the electron is assigned to the corresponding phase of the RF excitation. The individual electron events are binned into a three-dimensional data set (x, y, p_n). As this procedure only works if m is a natural number, the RF frequency must be quantized as

$$f_{\mathrm{RF}} = \frac{1}{\tau k} \text{ with } k \in \mathbb{N}. \tag{2}$$

The position of the DLD behind the energy filter offers several advantages: i) The energy filter can be used to filter out contributions due to inelastic scattering such as valence core losses. Moreover, it would be possible to image processes at specific energy levels. ii) It is possible to achieve higher magnifications. iii) When other external stimuli like lasers are employed, an illumination of the detector with laser light can be avoided.

3. RESULTS AND DISCUSSION

3.1. Magnetic vortex core dynamics

The application of the DLD to time-resolved measurements was demonstrated by studying the real space motion of a magnetic vortex in a Py disk illuminated by a parallel electron beam. Magnetic vortices are ideal structures for such studies as a result of their simple geometry, stability and resonant dynamics [24–27]. In the present study, the magnetic vortex core was imaged in Lorentz mode using Fresnel defocus imaging (see Fig. 2a). The in-plane field of the magnetic vortex shown in Fig. 2b results in convergence of the electron beam due to the Lorentz force in an overfocus image. The magnetic vortex core was excited by using in-plane magnetic fields oscillating at microwave frequencies. In general, it is expected to follow an elliptical orbit at resonance, with its trajectory depending on the shape, size and material of the disk [28, 29].

Figure 2c shows real space snapshots of the motion of the magnetic vortex core at different phases of the excitation cycle for a frequency of ∼417 MHz, a power of 23 dBm and a static out-of-plane magnetic field of 18 mT. The applied power results in a magnetic field strength of ∼0.07 mT at the sample (see Supplementary Material for details). The parameters were chosen to maximize the motion of the magnetic vortex core, while being small enough to avoid switching of the core, which has been demonstrated to only require small in-plane fields [12]. A total integration time of 2 minutes was sufficient to resolve the full gyration, with individual snapshots corresponding to average time steps of 13 ps each. The background was removed by dividing each frame by an image without the sample after normalizing the counts to the total exposure time. Due to the defocus, the standard calibration of the DLD cannot be used. Hence, the conversion factor from pixel to nm is determined by measuring the size of the vortex core for several frequencies off-resonance and correlating it to a measurement of the core with a K2 detector and a known calibration. This method to calibrate the detector introduces an uncertainty of about 10% in the spatial domain. The snapshots reveal that the bright spot, which corresponds to the position of the magnetic vortex core, is displaced between successive phases of the excitation cycle and follows a clockwise trajectory. The position of the magnetic vortex core at each step of the excitation cycle was determined by finding the center of mass of the brightest pixels. Its trajectory was recorded at several

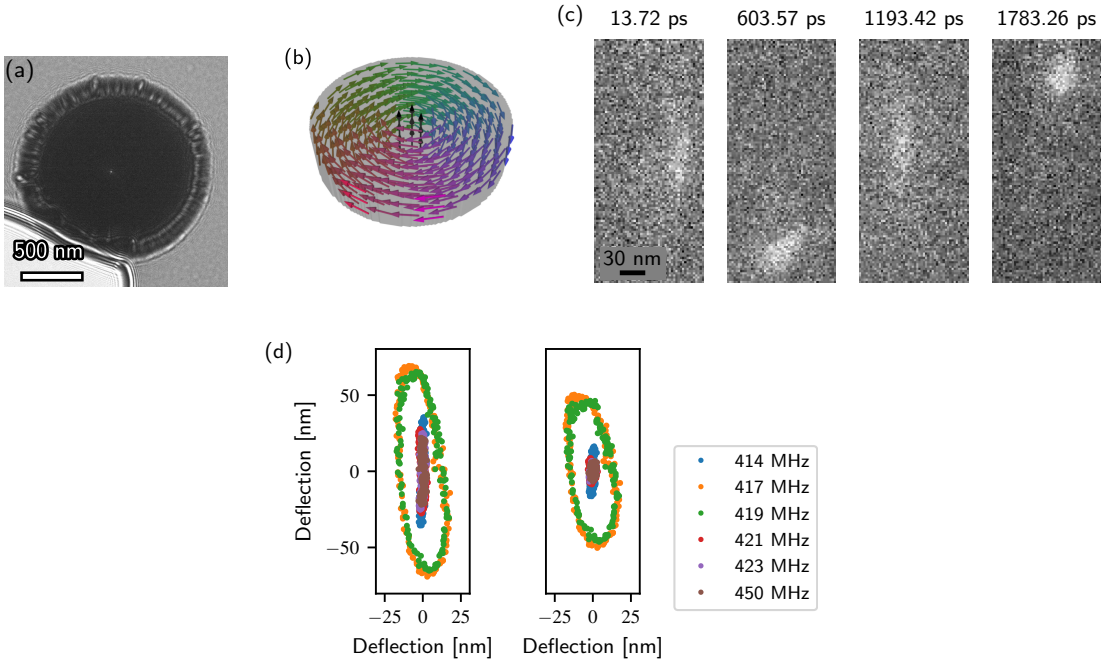

FIG. 2: Magnetic vortex core gyration. (a) Fresnel defocus image of a permalloy disk recorded in Lorentz mode at a defocus of 1 mm recorded with a K2 detector. The bright spot in the center indicates the position of the vortex core. The bright region at the lower left edge is a cut in the supporting membrane. (b) Schematic image of a magnetic vortex state with clockwise rotation and a core pointing upwards. (c) Snapshots of magnetic vortex core motion recorded at different time steps over 13 ps during excitation at 417 MHz in an 18 mT static out-of-plane applied magnetic field. The images reveal clockwise motion of the magnetic vortex core. They have been binned by a factor of 4 in the x and y directions for better visibility. (d) Dependence of position of magnetic vortex core in each frame on applied frequency, showing measurements before (left) and after (right) correction by subtraction of the image shift due to the electron beam - microwave interaction. The resonant frequency of the magnetic vortex core is characterised by an increase in the amplitude of the gyration at 417 and 419 MHz. The x and y axes have the same scaling.

frequencies close to the frequency for which the displacement was greatest. The left plot in Fig. 2d shows the apparent position of the magnetic vortex core during a full excitation cycle for all frequencies. Technical limitations resulting in a distortion of the recorded image are compensated by applying the Brown-Conrady model [30] (see Supplementary Material for

details). In addition to the vortex core motion, the position depends on the interaction of the electron beam with the microwave magnetic field, which results in a shift of the complete image. The image shift can be described approximately as a frequency-dependent sinusoidal deflection (see Supplementary Material for details). The true position of the magnetic vortex core was obtained by subtracting the image shift from the total deflection. The dependence of the resulting magnetic vortex core motion on applied frequency is shown in the right plot in Fig. 2d. There is a sharp resonance between 417 and 419 MHz, with the magnetic vortex core motion then following an elliptical trajectory. There, the deflection of the vortex core corresponds to about 23 ± 3 nm in x direction. Based on the elliptical trajectory, it can be excluded that the measured motion is purely an effect of the electron beam interaction with the RF fields as latter would result in a linear deflection (see Supplementary Material for details).

The experimental results were compared with simulations based on the LLG equation obtained using MuMax^3 software [31, 32]. The simulations were performed for a disk with a diameter of $d = 1.675\,\mu$m and a thickness of $t = 160$ nm, an exchange stiffness of $A_{ex} = 1.32 \cdot 10^{11}\,\frac{\mathrm{J}}{\mathrm{m}}$, a saturation magnetization of $M_S = 8 \cdot 10^5 \frac{A}{m}$, a g-factor of $\gamma_{LL} = 2.1 \cdot \frac{\mu_B}{\hbar}$, a damping coefficient of $\alpha = 0.016$, an applied out-of-plane magnetic field of 20 mT and an in-plane oscillating magnetic field with an amplitude of 0.1 mT. Figure 3 shows the results of the simulations, which reveal a sharp resonant frequency at 400 MHz, in good agreement with the experimental results. The inset to Fig. 3 shows the simulated trajectory of the magnetic vortex core in the disk. The transient period of a few ns that the magnetic vortex core requires to reach a stationary resonant trajectory is not included in the figure. The simulations reveal a slightly elliptical trajectory with a diameter of around 20 nm. This diameter is in good agreement with the experimental measured deflection in x direction. Discrepancies in the shape of the trajectories between the simulations and experimental results may result from inadequate correction for the electron beam - electromagnetic field interaction in the experiment, which does not take the frequency-dependent formation of standing waves in the holder into account. Moreover, the microwave field may not have the properties expected for an ideal waveguide [33]. In future experiments, these factors can be separated from the vortex core motion, *e.g.*, by imaging the deflection of a non-magnetic marker structure under microwave excitation and subsequently subtract it from the vortex core motion. Overall, the comparison between the simulations and the experimental results

confirms that dynamics occurring on a length scale of a few tens of nm are accessible using the DLD, while retaining the imaging capabilities of the TEM.

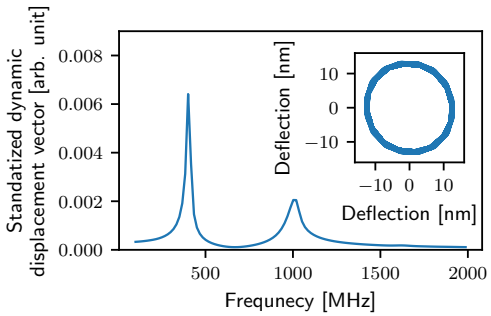

FIG. 3: Simulation of characteristics of magnetic vortex core dynamics, showing resonances at 400 and 1000 MHz. The stationary trajectory of the motion of the magnetic vortex core is shown in the inset for a frequency of 400 MHz.

3.2. Temporal resolution

Further prospects of combining a DLD with a TEM were investigated by determining the highest frequency that can be applied during imaging and the temporal resolution of the setup. For this purpose, the electron beam was positioned to illuminate only the SiN membrane and not the Py disk. The electron beam was then deflected only by its interaction with the microwave field introduced by the specimen holder *via* the Lorentz force. The deflection was imaged using low angle diffraction (LAD) [34]. A high camera length of 115 m was used to compensate for the small deflection angle of 41 μrad and to concentrate the incident illumination onto a spot on the detector. The spot size of the beam on the detector was $\sim$300 pixels^2. The deflection of the beam followed the phase of the excitation, with the spot undergoing sinusoidal motion parallel to the specimen holder axis. The total power of the excitation was chosen to be 17 dBm, which was sufficient to induce a resolvable deflection.

Figure 4 shows the time-integrated trajectory of the electron beam for different applied frequencies. Data reduction was performed by combining varying numbers of frames for each phase into snapshots of 8 frames for 100 MHz and 2 frames for measurements between 500 MHz and 1.5 GHz. For higher frequencies, data reduction was not applied. After removing the background and a distortion correction (see Supplementary Material for details), all

(x, y, p_n) datasets were smoothed using a Gaussian filter with $\sigma = 2$ pixels and rotated so that the primary axis of motion was parallel to the y axis. Each dataset was then cropped in the spatial domain to include only the deflected beam, as shown in Fig. 4. The sinusoidal motion can be seen in the time domain when summing over the x axis. The deflection does not follow the expected straight line, but is distorted. The bending of the deflections is thought to originate from remaining distortions of the recorded image (see Supplementary Material for details). The faint, dark lines at the bottom of the image integrated over the phase in Fig. 4a are a result of the distortion correction.

The highest resolvable frequency was determined by taking a linescan through the phase domain. The position of the linescan was chosen to be in the center of the deflection. The highest resolvable frequency corresponds to the condition when two points of maximum deflection can be distinguished, *i.e.*, when two peaks are present in the linescan. The position of the linescans is marked by a red line in Fig. 4. Figure 5a shows linescans for various frequencies. The condition that the two peaks need to be distinguishable is fulfilled up to ∼2.314 GHz. The temporal resolution for the different frequencies is defined as the full width at half maximum (FWHM) of the linescans. Figure 5b shows the FWHM of the broadest peak in the linescan for each frequency. The experimentally measured temporal resolution τ_{exp} is affected by the intrinsic temporal resolutions τ_i as well as the finite spot size of the electron beam τ_{spot}. In order to differentiate both effects, the sum of τ_i and τ_{spot} is fitted to τ_{exp}. Here, it is assumed that $\tau_{spot} = c/f_{RF}$ where c is constant. The intrinsic temporal resolution is as small as ∼122 ps. The intrinsic temporal is limited by several factors: the time spread of the microchannel plate, the accuracy of the TDC as well as the jitter of the frequency divider. We optimized the frequency divider for low jitter; the estimate of the jitter from the used components in the signal path is around 5 ps. The main factor determining the intrinsic time resolution is likely the DLD. It consists of the resolution of the TDC (30 ps), amplitude-to-time conversion in the discriminators and the time spread of the microchannel plate. For the time spread, values ranking from 30 ps [35] up to 150 ps [36] are reported in literature. DLDs of our type achieved 185 ps temporal resolution in photoelectron spectroscopy experiments [37].

The experiments performed in diffraction mode indicate that it is possible to perform dynamic measurements at frequencies of up to 2.3 GHz in the TEM using the present combination of a DLD and a microwave specimen holder with a temporal resolution of ∼122 ps.

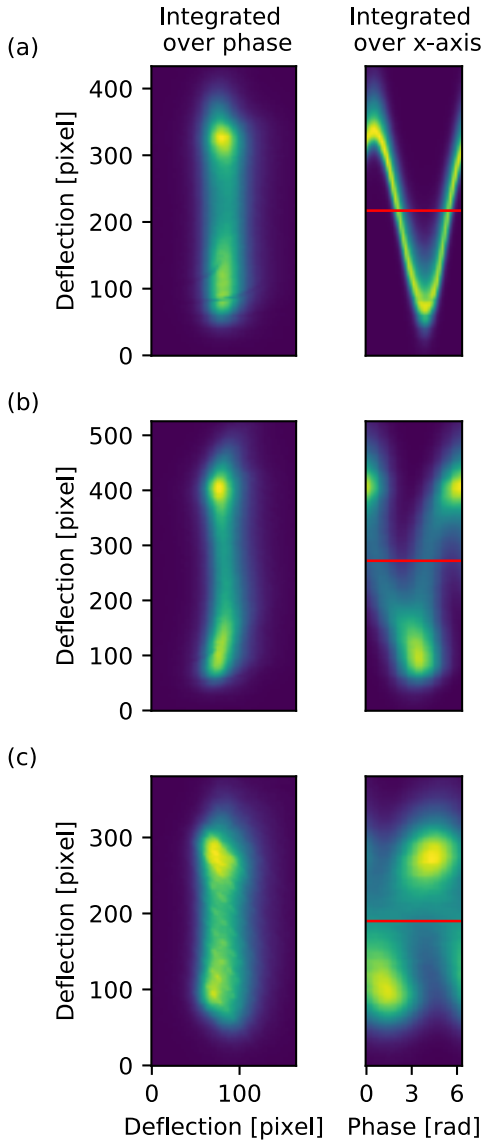

FIG. 4: Deflection of the electron beam by a microwave magnetic field visualized using low angle diffraction. The (x, y, p_n) datasets reveal sinusoidal motion for various frequencies: (a) $\sim$0.1 GHz, (b) $\sim$1.5 GHz and (c) $\sim$2.5 GHz. Integration over the different phases and the x axis are shown in the left and right columns, respectively. The red line marks the position where a linescan was extracted.

This temporal resolution allows dynamic processes to be resolved up to the lower GHz regime.

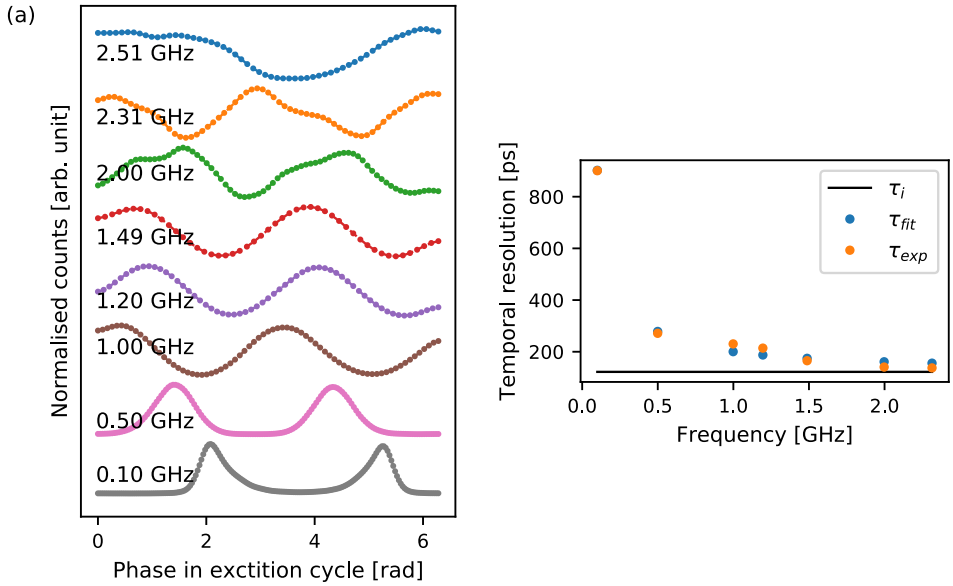

FIG. 5: Estimation of usable frequency range and temporal resolution. (a) Linescans recorded along the time domain of the integrated data over x for varying frequencies. Two peaks can be differentiated up to 2.3 GHz, suggesting that a sinusoidal motion is present and dynamic measurements can be performed up to this frequency. (b) FWHM τ_{exp} of the largest peak for the respective frequencies. τ_{fit} is a fit to τ_{expt} with contributions from τ_i and the effect of the spot size. The intrinsic spot size is ∼122 ps.

3.3. Discussion

The results presented in this paper demonstrate the use of a DLD to provide access to temporal resolutions in the ps regime for a variety of dynamic processes, while making use of the full imaging potential of transmission electron microscopy. The technique is not limited to mapping magnetic properties, but can be applied in either real or diffraction space to studies of dynamic changes introduced by a variety of stimuli. The electronics of the DLD can be synchronized to different stimuli, such as lasers.

Although approaches based on ultrafast TEM provide access to various dynamic processes [16, 38–41], they require a highly specialized or modified illumination system of the microscope. They may also compromise the quality of the electron beam, resulting in a low number of electrons per pulse [42] or beam displacement and blurring [43].

A key advantage of employing a DLD is the simplicity with which an existing microscope can be upgraded to achieve temporal resolution without the need for major modification and without compromising the quality of the electron beam or electron optics. It is only necessary to implement an additional camera or to exchange an existing one. In addition, the sample is imaged continuously, meaning that every electron can be recorded, thereby synchronized the electron dose and total measurement time. As the DLD is a single electron detection camera, the arrival time of each electron is measured. The technique is suited primarily to stroboscopic measurements to obtain sufficient contrast, just as for other ultrafast TEM approaches. The temporal resolution is currently limited to the ps regime as discussed in Sec. 3 3.2. Nevertheless, DLDs improve temporal resolution by six orders of magnitudes compared to most current TEM techniques. The benefit of the improved time resolution must be weighed against the degradation in terms of spatial resolution compared these techniques. Nevertheless, the loss in terms of spatial resolution can be encountered by using higher magnifications at the cost of a reduced field of view. Therefore, a DLD can only be applied to experiments which do not require very good spatial resolution and large field of views at the same time. Other detectors, which aim towards ps temporal resolution, while maintaining a high electron dose and closing the gap in terms of spatial resolution, are under development confirming the high interest in improving temporal resolution in TEM measurements. One example is the Timepix 4 [44].

4. CONCLUSIONS

We have presented two proof-of-principle experiments, one in real space and one in diffraction space, which provide insight into the use of a delay line detector for time-resolved transmission electron microscopy. An external stimulus was provided by using a magnetizing specimen holder to introduce gyration of a magnetic vortex core and deflection of the electron beam. In real space, gyration of the magnetic vortex core was studied in terms of its resonance frequency, with resonance spectra resolved by imaging its motion. Low angle diffraction experiments showed that it is possible to image the deflection of the electron beam up to frequencies of 2.3 GHz, while achieving a temporal resolution down to ∼122 ps. The full potential of this combination can be explored in future experiments by imaging other sample properties in the presence of different stimuli.

ACKNOWLEDGMENTS

We are grateful to Werner Pieper, Alexander Clausen and Alexander Müller for help with instrumentation and to Thibaud Denneulin for supporting experiments. In addition, we thank Rolf Speen and Philipp Kükenbrink for technical help in developing the magnetizing holder and Ralf Meckenstock and Ulrich Poppe for helpful discussions. Furthermore, we acknowledge Michael Farle for helpul input and discussion. This work is supported by the Deutsche Forschungsgemeinschaft (DFG) through CRC/TRR 270 (Project ID 405553726), the European Union's Horizon 2020 Research and Innovation Programme (Grant No. 856538, project "3D MAGiC" and Grant No. 823717, project "ESTEEM3") and ETH Zurich. The authors are grateful for funding from the Innovation Pool for the Joint Laboratory for Model and Data Driven Material Characterization in the Helmholtz Association. K. M.-C. acknowledges funding from the Impuls and Vernetzungsfond under contract VH-NG-1317.

SUPPLEMENTAL INFORMATION

See supplemental material for (1) videos of the vortex core gyration, (2) estimation of themicrowave magnetic field, (3) interaction of the microwave field and the electron beam, and(4) image distortions

CONTRIBUTIONS

TW, SD, YM, BZ, VM, AO, KMC, YA and REDB conceived the project and designed the experiments. TW, SD, YM, BZ, VM, PHL, AO, KMC and YA carried out the experiments. SF and MK prepared the sample. TW and SD analysed the experimental results, with support from YM, VM, AK and YA. BZ and SD performed the micromagnetic simulations. The manuscript was prepared by TW, SD, YM, YA, AK, KMC and REDB. All authors discussed the results and commented on the manuscript.

DECLARATION OF COMPETING INTEREST

The authors declare that they have no known competing financial interests or personal relationships that could have appeared to influence the work reported in this paper.

[1] S. S. Parkin, M. Hayashi, and L. Thomas, *Magnetic domain-wall racetrack memory*, Science **320**, 190 (2008).

[2] B. W. Zingsem, T. Feggeler, A. Terwey, S. Ghaisari, D. Spoddig, D. Faivre, R. Meckenstock, M. Farle, and M. Winklhofer, *Biologically encoded magnonics*, Nature communications **10**, 1 (2019).

[3] S. Wintz, V. Tiberkevich, M. Weigand, J. Raabe, J. Lindner, A. Erbe, A. Slavin, and J. Fassbender, *Magnetic vortex cores as tunable spin-wave emitters*, Nat. Nanotechnol. **11**, 948 (2016).

[4] A. S. Jenkins, L. S. E. Alvarez, P. P. Freitas, and R. Ferreira, *Digital and analogue modulation and demodulation scheme using vortex-based spin torque nano-oscillators*, Sci. Rep. **10**, 1 (2020).

[5] P. Fischer, G. Denbeaux, T. Ono, t. Okuno, T. Eimüller, D. Goll, and G. Schütz, *Magnetic soft X-ray transmission microscopy*, Curr. Opin. Solid State Mater. Sci. **7**, 173 (2003).

[6] W. Chao, P. Fischer, T. Tyliszczak, S. Rekawa, E. Anderson, and P. Naulleau, *Real space soft x-ray imaging at 10 nm spatial resolution*, Opt. Express **20**, 9777 (2012).

[7] R. Frömter, F. Kloodt, S. Rößler, A. Frauen, P. Staeck, D. R. Cavicchia, L. Bocklage, V. Röbisch, E. Quandt, and H. P. Oepen, *Time-resolved scanning electron microscopy with polarization analysis*, Appl. Phys. Lett. **108**, 142401 (2016).

[8] A. Kovács and R. E. Dunin-Borkowski, in *Handbook of Magnetic Materials*, Vol. 27 (Elsevier, 2018) pp. 59–153.

[9] M. Krajnak, D. McGrouther, D. Maneuski, V. O'Shea, and S. McVitie, *Pixelated detectors and improved efficiency for magnetic imaging in STEM differential phase contrast*, Ultramicroscopy **165**, 42 (2016).

[10] P. W. Hawkes and J. C. Spence, *Springer Handbook of microscopy* (Springer Nature, 2019).

[11] S. J. Gamble, M. H. Burkhardt, A. Kashuba, R. Allenspach, S. S. P. Parkin, H. C. Siegmann, and J. Stöhr, *Electric field induced magnetic anisotropy in a ferromagnet*, Phys. Rev. Lett.

102, 217201 (2009).

[12] B. Van Waeyenberge, A. Puzic, H. Stoll, K. Chou, T. Tyliszczak, R. Hertel, M. Fähnle, H. Brückl, K. Rott, G. Reiss, *et al.*, *Magnetic vortex core reversal by excitation with short bursts of an alternating field*, Nature **444**, 461 (2006).

[13] X. Shi, P. Fischer, V. Neu, D. Elefant, J. C. T. Lee, D. A. Shapiro, M. Farmand, T. Tyliszczak, H.-W. Shiu, S. Marchesini, S. Roy, and S. D. Kevan, *Soft x-ray ptychography studies of nanoscale magnetic and structural correlations in thin smco5 films*, Appl. Phys. Lett. **108**, 094103 (2016).

[14] D. J. Flannigan and A. H. Zewail, *4D Electron Microscopy: Principles and Applications*, Acc. Chem. Res **45**, 1828 (2012).

[15] L. Piazza, D. Masiel, T. LaGrange, B. Reed, B. Barwick, and F. Carbone, *Design and implementation of a fs-resolved transmission electron microscope based on thermionic gun technology*, Chem. Phys. **423**, 79 (2013).

[16] A. Feist, N. Bach, N. Rubiano da Silva, T. Danz, M. Möller, K. E. Priebe, T. Domröse, J. G. Gatzmann, S. Rost, J. Schauss, *et al.*, *Ultrafast transmission electron microscopy using a laser-driven field emitter: Femtosecond resolution with a high coherence electron beam*, Ultramicroscopy **176**, 63 (2017).

[17] J. Yang, Y. Yoshida, and H. Yasuda, *Ultrafast electron microscopy with relativistic femtosecond electron pulses*, Microscopy **67**, 291 (2018).

[18] A. Oelsner, O. Schmidt, M. Schicketanz, M. Klais, G. Schönhense, V. Mergel, O. Jagutzki, and H. Schmidt-Böcking, *Microspectroscopy and imaging using a delay line detector in time-of-flight photoemission microscopy*, Rev. Sci. Instrum. **72**, 3968 (2001).

[19] D. Jannis, K. Müller-Caspary, A. Béché, A. Oelsner, and J. Verbeeck, *Spectroscopic coincidence experiments in transmission electron microscopy*, Appl. Phys. Lett. **114**, 143101 (2019).

[20] B. Zingsem, *Pico-second spin dynamics in nano-structures: Towards nanometer spatial resolution by Transmission electron microscopy*, Ph.D. thesis, Universität Duisburg-Essen (2020).

[21] C. Boothroyd, A. Kovács, and K. Tillmann, *FEI Titan G2 60-300 HOLO*, Journal of large-scale research facilities **2**, 44 (2016).

[22] S. Finizio, S. Wintz, D. Bracher, E. Kirk, A. S. Semisalova, J. Förster, K. Zeissler, T. Weßels, M. Weigand, K. Lenz, *et al.*, *Thick permalloy films for the imaging of spin texture dynamics in perpendicularly magnetized systems*, Phys. Rev. B **98**, 104415 (2018).

[23] Frequency divider, https://github.com/eduphys/frequency-divider.

[24] S.-B. Choe, Y. Acremann, A. Scholl, A. Bauer, A. Doran, J. Stöhr, and H. A. Padmore, *Vortex core-driven magnetization dynamics*, Science **304**, 420 (2004).

[25] R. Antos, Y. Otani, and J. Shibata, *Magnetic vortex dynamics*, J. Phys. Soc. Jpn. **77**, 031004 (2008).

[26] N. Rubiano da Silva, M. Möller, A. Feist, H. Ulrichs, C. Ropers, and S. Schäfer, *Nanoscale Mapping of Ultrafast Magnetization Dynamics with Femtosecond Lorentz Microscopy*, Phys. Rev. X **8**, 031052 (2018).

[27] M. Möller, J. H. Gaida, S. Schäfer, and C. Ropers, *Few-nm tracking of current-driven magnetic vortex orbits using ultrafast Lorentz microscopy*, Comm. Phys. **3**, 1 (2020).

[28] K. Y. Guslienko, B. Ivanov, V. Novosad, Y. Otani, H. Shima, and K. Fukamichi, *Eigenfrequencies of vortex state excitations in magnetic submicron-size disks*, J. Appl. Phys. **91**, 8037 (2002).

[29] V. Novosad, F. Y. Fradin, P. E. Roy, K. S. Buchanan, K. Y. Guslienko, and S. D. Bader, *Magnetic vortex resonance in patterned ferromagnetic dots*, Phys. Rev. B **72**, 024455 (2005).

[30] C. Brown, *Close range camera calibration, symposium on close range photogrammetry*, Photogramm. Eng. Remote. Sens. **8**, 855–866 (1971).

[31] A. Vansteenkiste, J. Leliaert, M. Dvornik, M. Helsen, F. Garcia-Sanchez, and B. Van Waeyenberge, *The design and verification of Mumax3*, AIP Adv. **4**, 107133 (2014).

[32] L. Exl, S. Bance, F. Reichel, T. Schrefl, H. Peter Stimming, and N. J. Mauser, *LaBonte's method revisited: An effective steepest descent method for micromagnetic energy minimization*, J. Appl. Phys. **115**, 17D118 (2014).

[33] D. M. Pozar, *Microwave engineering* (John wiley & Sons, 2011).

[34] F. Goncalves, G. Paterson, D. McGrouther, T. Drysdale, Y. Togawa, D. Schmool, and R. Stamps, *Probing microwave fields and enabling in-situ experiments in a transmission electron microscope*, Scientific reports **7**, 1 (2017).

[35] D. A. Debrah, G. A. Stewart, G. Basnayake, A. Nomerotski, P. Svihra, S. K. Lee, and W. Li, *Developing a camera-based 3d momentum imaging system capable of 1 mhits/s*, Review of Scientific Instruments **91**, 023316 (2020).

[36] M. Huth, C.-T. Chiang, A. Trützschler, F. O. Schumann, J. Kirschner, and W. Widdra, *Electron pair emission detected by time-of-flight spectrometers: Recent progress*, Applied Physics

Letters **104**, 061602 (2014).

[37] M. H. Berntsen, O. Götberg, and O. Tjernberg, *An experimental setup for high resolution 10.5 ev laser-based angle-resolved photoelectron spectroscopy using a time-of-flight electron analyzer*, Review of Scientific Instruments **82**, 095113 (2011).

[38] J. C. Williamson, J. Cao, H. Ihee, H. Frey, and A. H. Zewail, *Clocking transient chemical changes by ultrafast electron diffraction*, Nature **386**, 159 (1997).

[39] X. Fu, E. Wang, Y. Zhao, A. Liu, E. Montgomery, V. J. Gokhale, J. J. Gorman, C. Jing, J. W. Lau, and Y. Zhu, *Direct visualization of electromagnetic wave dynamics by laser-free ultrafast electron microscopy*, Sci. Adv. **6**, eabc3456 (2020).

[40] J. W. Lau, K. B. Schliep, M. B. Katz, V. J. Gokhale, J. J. Gorman, C. Jing, A. Liu, Y. Zhao, E. Montgomery, H. Choe, *et al.*, *Laser-free GHz stroboscopic transmission electron microscope: Components, system integration, and practical considerations for pump–probe measurements*, Rev. Sci. Instrum. **91**, 021301 (2020).

[41] J. Van Rens, W. Verhoeven, E. Kieft, P. Mutsaers, and O. Luiten, *Dual mode microwave deflection cavities for ultrafast electron microscopy*, Appl. Phys. Lett. **113**, 163104 (2018).

[42] F. Houdellier, G. Caruso, S. Weber, M. Hÿtch, C. Gatel, and A. Arbouet, *Optimization of off-axis electron holography performed with femtosecond electron pulses*, Ultramicroscopy **202**, 26 (2019).

[43] L. Zhang, M. W. Garming, J. P. Hoogenboom, and P. Kruit, *Beam displacement and blur caused by fast electron beam deflection*, Ultramicroscopy **211**, 112925 (2020).

[44] M. Campbell, J. Alozy, R. Ballabriga, E. Frojdh, E. Heijne, X. Llopart, T. Poikela, L. Tlustos, P. Valerio, and W. Wong, *Towards a new generation of pixel detector readout chips*, J. Instrum. **11** (01), C01007.

Supplemental information for: "Continuous illumination picosecond imaging using a delay line detector in a transmission electron microscope"

Teresa Weßels,[1,2] Simon Däster,[3] Yoshie Murooka,[1] Benjamin Zingsem,[4] Vadim Migunov,[1,5] Maximilan Kruth,[1] Simone Finizio,[6] Peng-Han Lu,[1] András Kovács,[1] Andreas Oelsner,[7] Knut Müller-Caspary,[1] Yves Acremann,[3] and Rafal E. Dunin-Borkowski[1]

[1]*Ernst Ruska-Centre for Microscopy and Spectroscopy with Electrons and Peter Grünberg Institute, Forschungszentrum Jülich, 52425 Jülich, Germany*

[2]*Lehrstuhl für Experimentalphysik IV E, RWTH Aachen University, 52056 Aachen, Germany*

[3]*Laboratory for Solid State Physics, ETH Zurich, 8093 Zurich, Switzerland*

[4]*Faculty of Physics and Center for Nanointegration (CENIDE), University of Duisburg-Essen, 47057 Duisburg, Germany*

[5]*Central Facility for Electron Microscopy (GFE), RWTH Aachen University, 52074 Aachen, Germany*

[6]*Swiss Light Source, Paul Scherrer Institut, 5232 Villigen PSI, Switzerland*

[7]*Surface Concept GmbH, 55124 Mainz, Germany*

1. VIDEOS OF MAGNETIC VORTEX CORE GYRATION

Videos of magnetic vortex core gyration at 414, 417, 419, 421, 424, and 450 MHz are available as additional Supplementary Material. They show largely unprocessed data, in which only the contrast has been adjusted to make the magnetic vortex core visible.

2. ESTIMATION OF MICROWAVE MAGNETIC FIELD

The strength of the microwave magnetic fields was estimated based on its interaction with the electron beam. The deflection of the electrons due to this interaction was imaged using low angle diffraction on a standard charge-coupled device camera [1]. The deflection angle θ can be correlated to the applied field $B_\perp$ *via* the expression

$$\theta = \frac{e\lambda}{h} B_\perp t \quad , \tag{1}$$

where e is the electron charge, $\lambda = 2\,\mathrm{pm}$ is the electron wavelength at an accelerating voltage of 300 kV and h is Planck's constant [2]. The thickness t of the cartridge is $\sim$500 μm. The deflection is measured to be 16 μrad for an applied RF current at 418 MHz and 23 dBm (see Fig. 1). Hence, the magnetic field is estimated to be $\sim$0.07 mT. The presence of a bright spot in Fig. 1 results from a part of the RF current being reflected back to the frequency generator and the generator turns off for a short time. During this time no microwave fields are applied and the electron beam is located at the center. In contrast to the magnetic fields, a deflection due to the induced electric fields is not expected as the holder is designed in such a way that they are aligned parallel to the electron beam direction [3]. The absence of in-plane electric fields is experimentally confirmed by the pure linear deflection of the electron beam due to the microwave fields imaged with LAD (see Fig. 1).

When applying Eq. 1, it is assumed that the magnetic field in the cartridge is uniform and that there are no stray fields. Both assumptions are likely to result in an underestimation of the magnetic field, since it is strongest at the sample position. There are likely to be stray fields outside of the cartridge that deflect the electron beam in the opposite direction than the fields in the cartridge. Although the field depends on applied frequency, it does not change strongly over the frequency range of the magnetic vortex core gyration, since the resonant frequency is constrained to a small range.

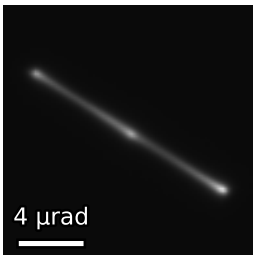

FIG. 1: Deflection of the electron beam due to a microwave magnetic field at 418 MHz and 23 dBm applied power imaged using low angle diffraction on a charge-coupled device camera. The bright spot in the center results from reflection of the RF current into the RF generator.

3. INTERACTION OF THE MICROWAVE FIELD AND THE ELECTRON BEAM

Due to the Lorentz force, the microwave field does not only interact with the sample, but also with the electron beam itself. The magnetic microwave field therefore creates an image shift out of focus (see Fig. 2a). As the microwave excitation is sinusoidal, the deflection also takes on a sinusoidal shape. This knowledge can be used to correct for the image shift, according to the equation

$$\begin{aligned} y_1 &= y_0 + y' \\ y_0 &= y_1 - y' = y_1 - [a \cdot sin(b \cdot t + c) + d] \quad , \end{aligned} \tag{2}$$

where it is assumed for simplicity that the beam is purely deflected along the y axis. The deflected coordinate y_1 can be obtained by adding the deflection y' to the non-deflected coordinate y_0. The parameter a corresponds to the amplitude of the deflection. The remaining parameters are required to match the phase and offset.

The parameters needed for correction were determined by using the following procedure:

1. The dataset at 450 MHz was assumed to be out of resonance, with the magnetic vortex core stationary in the disk. The movement of the core in the images was then assumed to be purely due to the electron beam interaction. After rotating the image so that the primary axis of motion was along the y axis, a sinusodial function was fitted to the dependence of the magnetic vortex core position on time. This fit provided the beam deflection y'. When subtracting it from the experimental dataset, one can obtain

the parameter y_0. The amplitude of the beam shift is used to determine the shift for all other frequencies and corresponds to the parameter a in Eq. 2. The parameters b, c and d are needed to match the phase in the excitation cycle. Figure 2b shows the correction for the deflection at 450 MHz.

2. In the next step, the magnetic vortex core movement at different frequencies was studied. Each dataset was rotated so that the primary movement followed the y axis by using the rotation angle determined for 450 MHz. Sinusoidal functions were fitted to them to determine the parameters b, c and d to match the phase and offset. In this way, all of the parameters describing the beam deflection due to the microwave-beam interaction could be determined.

In the final step, the image shift due to interaction of the microwave and the electron beam was removed from every dataset by subtracting image shift from the movement of the magnetic vortex core using the amplitude a of the interaction determined at 450 MHz and the phase parameters b, c and d determined at each frequency.

4. IMAGE DISTORTIONS

Images recorded using the DLD were distorted due to issues with the control electronics of the imaging filter. As a result, straight lines in the images appeared bent, as shown in an image of a standard calibration sample with a lattice spacing of ∼480 nm in Fig. 3a. In addition to distortions, it was not possible to illuminate the full area of the DLD. These image distortions were corrected applying the Brown-Conrady model [4] which can take tangential as well as radial distortions into account. Figure 3b shows the image of the calibration sample after distortion correction. Even though the distortions were not fully removed, the degree of bending is reduced.

[1] F. Goncalves, G. Paterson, D. McGrouther, T. Drysdale, Y. Togawa, D. Schmool, and R. Stamps, *Probing microwave fields and enabling in-situ experiments in a transmission electron microscope*, Scientific reports **7**, 1 (2017).

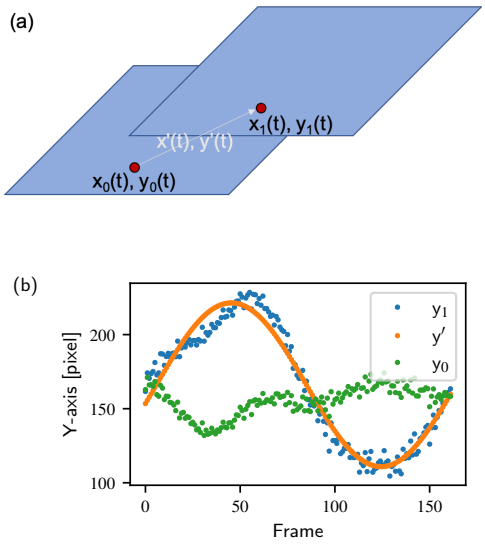

FIG. 2: Interaction of the microwave field and the electron beam. (a) Visualization of image shift due to the microwave field. The image is shifted depending on the phase of the excitation cycle and follows a sinusoidal motion. The position of the disk is marked in red and does not change in the image. However, its position shifts with the image and therefore also follows a sinusoidal motion. (b) Correction of image shift introduced by the microwave field of the holder. The blue dots represent the measured position of the vortex core. The orange dots show a sinusoid fitted to this motion. The green dots show motion of the magnetic vortex core after subtraction of the sinusoid.

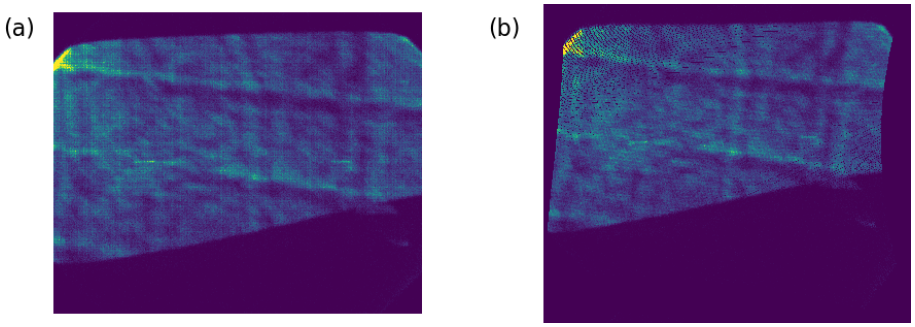

FIG. 3: Image of a calibration sample with a periodic lattice spacing. (a) Original image revealing distortion of the image due to electronic issues. (b) Calibration sample after correction of image distortions.

[2] A. Kovács and R. E. Dunin-Borkowski, in *Handbook of Magnetic Materials*, Vol. 27 (Elsevier, 2018) pp. 59–153.

[3] B. Zingsem, *Pico-second spin dynamics in nano-structures: Towards nanometer spatial resolution by Transmission electron microscopy*, Ph.D. thesis, Universität Duisburg-Essen (2020).

[4] C. Brown, *Close range camera calibration, symposium on close range photogrammetry*, Photogramm. Eng. Remote. Sens. **8**, 855–866 (1971).